MATERIALS CHEMISTRY FRONTIERS

RESEARCH ARTICLE

View Article Online
View Journal | View Issue

Cite this: *Mater. Chem. Front.*, 2023, **7**, 3668

Rational design of amphiphilic BODIPY-based photosensitizers for multimodal imaging-guided phototherapy†

Minling Jiang, Jinjin Zhang, Yaojun Li, Tingyu Shi, Tiantian Ma, Yiqi Sun, Huayu Qiu, Yang Li* and Shouchun Yin*

Received 6th March 2023,
Accepted 23rd May 2023

DOI: 10.1039/d3qm00239j

rsc.li/frontiers-materials

The design of effcient photosensitisers for cancer theranostics is of great importance, especially for multimodal-imaging-guided synergistic therapy. The key to achieving accurate imaging-guided phototherapy is to balance the energy distribution between fluorescence imaging, photodynamic therapy (PDT) and photothermal therapy (PTT). Herein, we propose a strategy of introducing hydrophilic chains and halogen atoms in boron dipyrromethene (BODIPY), which can self-assemble into *J*-aggregate nano-micelles in water with free BODIPY molecules in the cavity, enabling both imaging and multiple therapeutics. Remarkably, the degree of *J*-aggregation of the nanoparticles (NPs) varies under the influence of the steric effects of the 3,5-position group of BODIPY. In particular, BDPN NPs with suitable nano-size, strong NIR-absorption, applicable fluorescence quantum yield (Φ_f = 3.0%), satisfactory photothermal conversion efficiency (PCE = 54.9%) and favorable singlet oxygen quantum yield (Φ_Δ = 40.76%) were proved to completely destroy 4T1 tumors under 808 nm laser irradiation without significant dark cytotoxicity, enabling synergistic PDT/PTT guided by fluorescence/photothermal/photoacoustic imaging. This study provides an emerging strategy for cancer therapy and a novel idea for the future development of new efficient photosensitizers.

Introduction

Cancer is one of the most important health problems facing human beings, and how to carry out effective cancer diagnosis and treatment is a major challenge in the current biomedical field. Traditional therapeutic methods, such as surgery,[1] radiotherapy,[2] chemotherapy[3] and targeted therapy,[4] can effectively kill tumor cells, but they also have disadvantages including low targeting, lack of specificity, drug resistance and strong side effects. Therefore, it is urgent to find more effective, safe and reliable means of diagnosing and treating cancer. Since 1998, when John Funkhouser first introduced the concept of theranostics,[5] it has been developed into a new biomedical technology that integrates diagnosis or monitoring of disease with treatment. Compared with single diagnosis or treatment, theranostics has shown great potential for real-time monitoring and timely feedback of drug treatment process.[6–9]

Photodynamic therapy (PDT) has been widely studied in recent years as a novel cancer treatment with the advantages of non-invasiveness, high selectivity, excellent repeatability and low systemic cytotoxicity.[10–14] PDT is the production of cytotoxic reactive oxygen species (ROS) after light activation of non-toxic photosensitizers (PSs) in the tumor area, which has the ability to kill the tumor. Photosensitizer (PS) plays a major role in the process of PDT.[15] The mechanism is that after light activation, PS will interact with oxygen and hydrogen peroxide at the tumor site to produce cytotoxic ROS, such as singlet oxygen ($^1O_2$), superoxide anion ($O_2^{\bullet-}$), hydroxyl radical ($^\bullet OH$), *etc.*, which can kill the diseased cells and tissues to achieve therapeutic effects.[15–17] However, continuous PDT can rapidly deplete oxygen and exacerbate the tumor hypoxic microenvironment, which further leads to severe limitations of PDT.[18–20] To overcome this defect, PDT can be combined with other therapies, such as photothermal therapy (PTT),[21] chemotherapy (CT),[22,23] chemodynamic therapy,[24] and immunotherapy,[25] to achieve a mutually beneficial therapeutic effect. PS in the excited singlet state (S_1) can either reach the excited triplet state (T_1) and generate ROS for PDT through intersystem crossing (ISC), or return to the ground state (S_0) and generate heat for PTT through non-radiative transition, which can kill cancer cells by raising the local temperature of the tumor and make up

College of Material, Chemistry and Chemical Engineering, Hangzhou Normal University, Key Laboratory of Organosilicon Chemistry and Material Technology, Ministry of Education, Key Laboratory of Organosilicon Material Technology, Zhejiang Province, Hangzhou 310036, People's Republic of China.
E-mail: liyang@hznu.edu.cn, yinsc@hznu.edu.cn

† Electronic supplementary information (ESI) available. See DOI: https://doi.org/10.1039/d3qm00239j

for the dilemma of oxygen deprivation of PDT simultaneously. Moreover, PTT is usually accompanied by photothermal imaging (PTI) and photoacoustic imaging (PAI),[26–29] which provides a direction to design a PS with imaging capability and multiple phototherapeutic capabilities in one. Among various photosensitizers, boron dipyrromethane (BODIPY)[30–33] stands out for its better photostability, applicable fluorescence quantum yield and molar extinction coefficient, has been widely used in fluorescent probes,[34] biosensors[35] and bioimaging.[36] Through rational design, such as building D–A structures,[37] adjusting the degree and length of conjugation,[38] restricting conformational[39] and constructing *J*-aggregation,[40] the multiple sites of BODIPY can be modified to adjust wavelength to reach the near-infrared region (NIR), resulting in better tissue penetration and imaging ability. However, the generation of fluorescence usually attenuates its ISC and non-radiative transition, so a reasonable balance of the three processes is the key to obtain excellent theranostics efficiency.

Based on the above ideas, we designed and synthesized a series of iodine-containing hydrophilic BODIPYs with different electron donors (*N*,*N*-diethylphenyl, 1-methylindolyl, *N*-ethylcarbazolyl and julonidine) attached to the 3- and 5-positions of the BODIPY nuclei by the carbon–carbon double bonds to drive the wavelength to the near-infrared region (Scheme 1). Due to the introduction of iodine atoms and the hydrophilic interaction of hydrophilic chains, halogen bonding (XB) interactions[41,42] and π-stacking interactions[43] exist between molecules, which can self-assemble into anti-parallel *J*-aggregate forms in water.[44] The formation of *J*-aggregates can not only lead to redshift and strong NIR absorption, but also severely suppress fluorescence emission and ISC, resulting in the dissipation of most energy through non-radiative transition, which is conducive to the acquisition of PTT/PTI/PAI capabilities. Furthermore, due to the effect of the steric hindrance of the 3,5 sites of BODIPY and the iodine atom, the four

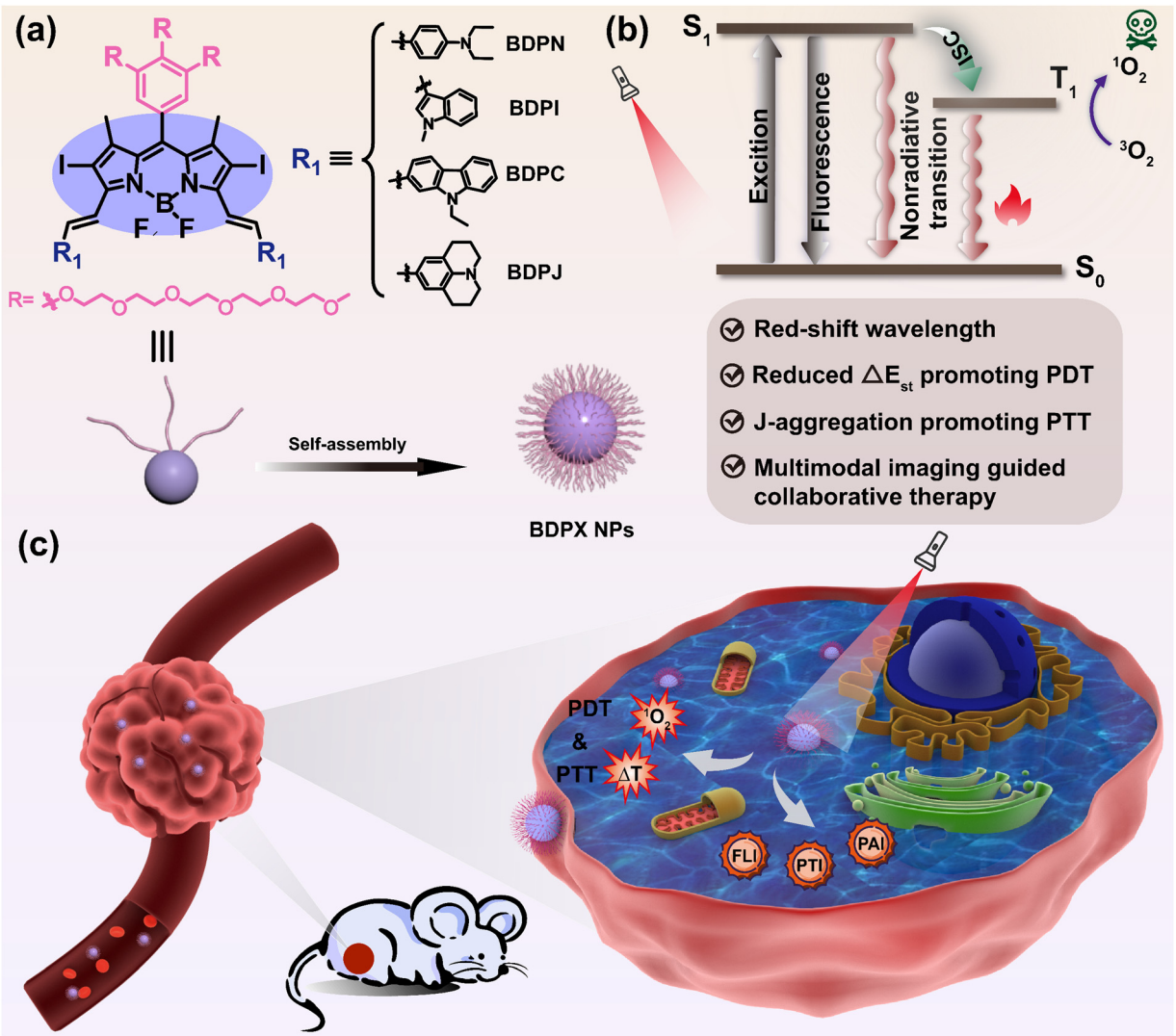

Scheme 1 The schematic representation of (a) amphiphilic iodine-containing BODIPY possessing different groups forming water-stable nanoparticles by self-assembly, (b) photophysical processes leading to fluorescence, $^1O_2$ and heat generation, and (c) synergistic phototherapy for multimodal imaging guidance *in vivo*.

as-prepared molecules formed different degrees of *J*-aggregation. Therefore, the obtained NPs not only have the ability of PTT, but also have PDT effect and fluorescence imaging ability. The properties of BDPN NPs, BDPI NPs, BDPC NPs and BDPJ NPs were examined by spectral characterisation, fluorescence quantum yield detection, photodynamic testing and photothermal testing. Promisingly, BDPN NPs, BDPC NPs and BDPJ NPs showed excellent fluorescence and phototherapeutic effects. The *in vitro* and *in vivo* tumor treatment and imaging effects of the above three NPs on 4T1 tumors were systematically investigated under 808 nm laser irradiation. The BDPN NPs with synergistic phototherapeutic ability not only efficiently destroyed 4T1 tumors, but also combined multiple imaging capabilities. This work proposed a nanotherapy system that can modulate the degree of conjugation and aggregation to obtain synergistic phototherapy with multimodal imaging guidance.

Results and discussion

Synthesis and characterization

The precursor compound iodine-containing BODIPY was prepared according to literature procedures.[45] Subsequently, a series of BODIPYs (BDPN/BDPI/BDPC/BDPJ) with D–A–D conjugated structures were synthesized by the Knoevenagel reaction, which connected various electron donors (*N*, *N*-diethylphenyl, 1-methylindole, *N*-ethylcarbazole and julonidine) to the 3- and 5-positions of the BODIBY core *via* a double bond bridge, and the detailed synthetic route can be found in Scheme S1 (ESI†). Then, the structures of the synthesized four compounds were characterized by ^{1}H NMR, ^{13}C NMR, ^{19}F NMR and HRMS (see ESI† for details). Through changing different electronic structures, the intramolecular charge transfer (ICT) and ISC ability can be systematically regulated. In order to investigate the rationality of the molecular design, the highest occupied molecular orbital (HOMO) and lowest unoccupied molecular orbital (LUMO) distributions and energy gaps (ΔE_{ST}) between the lowest excited singlet state and the lowest triplet state of the four compounds were researched by density functional theory (DFT) calculations (Fig. 1a). The absorption spectra (Fig. 1b) exhibited that the maximum absorption wavelengths of BDPN, BDPI, BDPC and BDPJ in CH_2Cl_2 were 755 nm, 724 nm, 698 nm and 791 nm, respectively, which were consistent with the theoretical calculations (Fig. 1b). Additionally, the molar extinction coefficient was calculated to be 9.64×10^4 M^{-1} cm^{-1} for BDPN, 4.17×10^4 M^{-1} cm^{-1} for BDPI, 8.31×10^4 M^{-1} cm^{-1} for BDPC and 3.42×10^4 M^{-1} cm^{-1} for BDPJ, which displayed a high light absorption and contributed to better light utilisation. According to the fluorescence spectra (Fig. 1c), BDPJ exhibits the maximum fluorescence emission of 924 nm compared to BDPN (853 nm), BDPI (773 nm), BDPC (739 nm), but its fluorescence quantum yield of 5.95% is significantly lower than that of BDPN (12.75%), BDPI (24.34%), BDPC (25.32%). The optical properties mentioned above could demonstrate their potential NIR fluorescence imaging capability. In addition, the small ΔE_{ST} also implied that the four compounds should have a good ROS generation capacity for effective photodynamic therapy.

Nanoparticle morphology and optical property

The introduction of long hydrophilic chains enabled the molecules to form NPs by self-assembly in water through hydrophilic and hydrophobic interactions. The critical aggregation concentrations (CAC) were calculated to be 1.61×10^{-5} M for BDPN, 1.44×10^{-5} M for BDPI, 1.47×10^{-5} M for BDPC, and 1.41×10^{-5} M for BDPJ (Fig. S18, ESI†). The morphology and size of these NPs prepared by self-assembly were determined by transmission electron microscopy (TEM) and dynamic light scattering (DLS). DLS data indicated that the average hydrodynamic sizes of BDPN NPs, BDPI NPs, BDPC NPs and BDPJ NPs were 153 nm, 96 nm, 145 nm and 246 nm, respectively (Fig. 1d, e and Fig. S21, ESI†). TEM images showed that all the four NPs had a homogeneous spherical morphology, but their sizes were slightly different from those of DLS. BDPN NPs, BDPC NPs, and BDPJ NPs all decreased in size by approximately 50 nm, possibly due to differences in hydrophilic chain spreading in water,[46] whereas the size of BDPI NPs increased by about 30 nm, which may be due to aggregation. The particle sizes of NPs were further tested after staying for several consecutive days, and BDPN NPs, BDPC NPs and BDPJ NPs showed slightly changes within seven days, demonstrating good particle size stability. While the particle size of BDPI NPs gradually increased, which may be induced by the occurrence of aggregation (Fig. 1f). Above all, these NPs with appropriate particle sizes allow potential passive targeting of tumors through enhanced permeability and retention (EPR) effects.[47]

Then, we investigated the photophysical properties of NPs in water. They all exhibited significant absorption redshift due to *J*-aggregation caused by the presence of hydrophilic chains and XB interactions (Fig. 1b). The maximum absorption peaks of BDPN NPs, BDPI NPs, BDPC NPs and BDPJ NPs in water were red-shifted to 860 nm, 798 nm, 737 nm and 800 nm, respectively. For example, BDPN exhibited a characteristic maximum absorption peak at 745 nm in pure THF. As the water fraction of the THF/water mixture was increased, the maximum absorption was red-shifted, and the new maximum absorption peak appeared at 860 nm in pure water with the absorption red-shift of 105 nm, demonstrating the *J*-aggregation of BDPN (Fig. 1g). However, the shoulder absorption peak at 745 nm was still observed which may be attributed to some of the free BDPN in the micelles formed by BDPN in water. Just like BDPN, the absorption of the other three NPs also showed varying degrees of redshift, suggesting that the introduction of different groups did lead to different degree of *J*-aggregation (Fig. S19, ESI†). The dihedral angles between the BODIPY nucleus and different groups at 3,5-positions were investigated by theoretical calculations as BDPN for 36.7 Å, BDPI for 28,72 Å, BDPC for 39.02 Å, BDPJ for 21.18 Å. The calculation of the dihedral angle showed that the larger the dihedral angle between the BODIPY nucleus and the different groups, the lower the degree of *J*-aggregation (Fig. S20, ESI†). Fluorescence quantum yields of BDPN NPs,

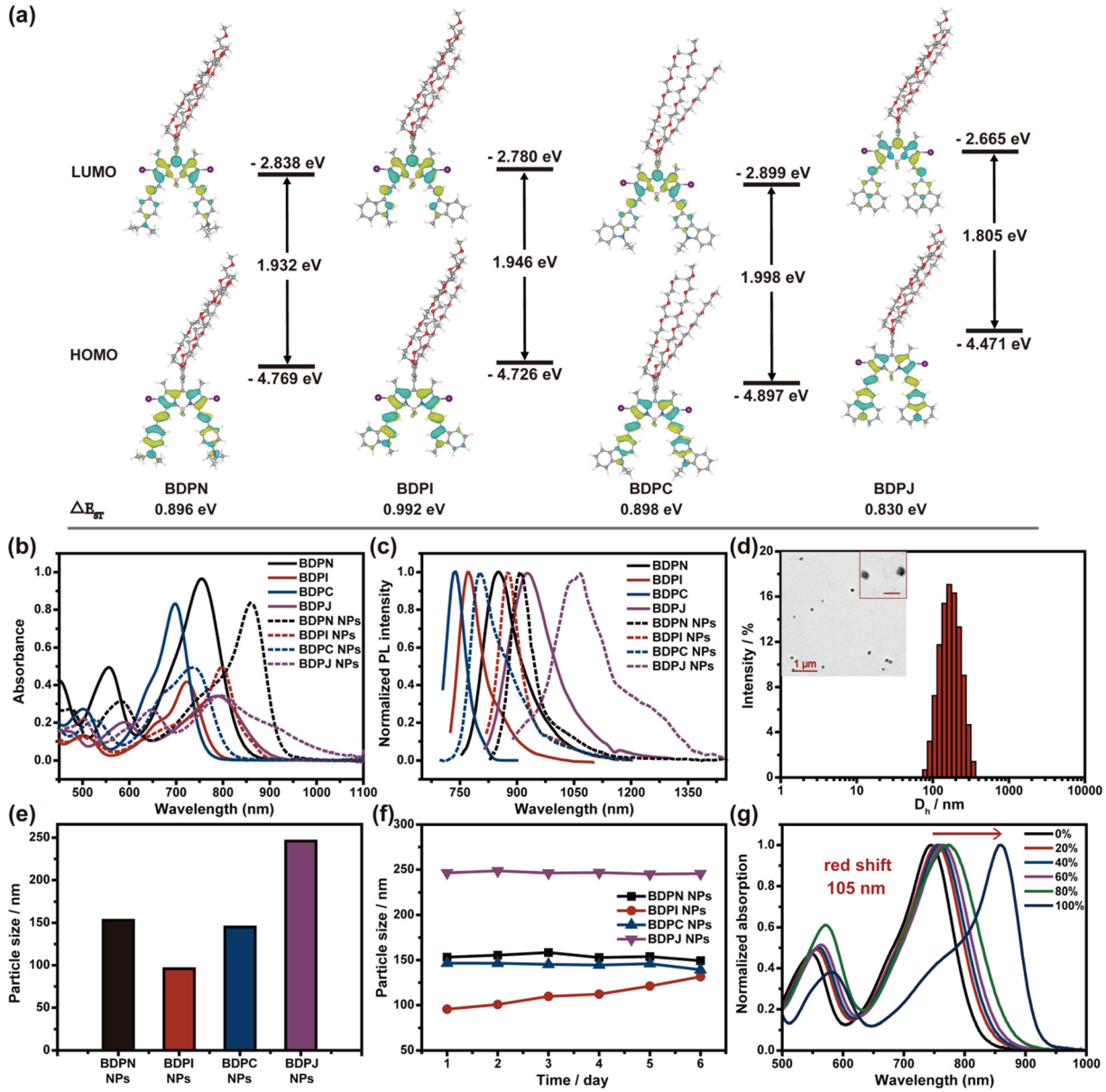

Fig. 1 (a) The optimized geometry and HOMO and LUMO orbitals acquired from DFT calculations (B3LYP) of BDPN, BDPI, BDPC and BDPJ in the ground state (S_0). (b) The absorption and (c) normalized fluorescence spectra of free molecules in CH_2Cl_2 and nanoparticles in water (10 μM). (d) The average hydrodynamic size of BDPN NPs (Insert: the TEM image of BDPN NPs. Scale bar: 200 nm). (e) The average hydrodynamic size and (f) dimensional stability of BDPN NPs, BDPI NPs, BDPC NPs and BDPJ NPs. (g) UV-vis spectra of BDPN in THF/water mixtures (10 μM).

BDPI NPs, BDPC NPs and BDPJ NPs were measured for 3.0%, 2.0%, 1.52% and 1.26%, respectively by the integrating sphere method. The formation of *J*-aggregation typically significantly inhibited the singlet radiative decay pathway, leading to restrict fluorescence emission. As shown in Fig. 1c, the maximum fluorescence emission wavelengths of BDPN NPs, BDPI NPs, BDPC NPs and BDPJ NPs were 910 nm, 877 nm, 804 nm and 1064 nm, respectively. Although fluorescence quantum yields had fallen dramatically compared to free molecules, NPs still showed imaging capability on account of NIR emission. Surprisingly, the emission of BDPJ NPs even reached the second near-infrared region (NIR-II, 1000–1700 nm). This excellent NIR florescence property allows these NPs to be tracked simultaneously during the phototherapy.

Photodynamic effect and photothermal performance

A good resistance to photobleaching is a prerequisite for effective phototherapy. To assess the photostability of BDPN NPs, BDPI NPs, BDPC NPs and BDPJ NPs, the absorbance at maximum absorption of NPs was monitored after being irradiated with 808 nm laser (0.5 W cm^{-2}). The absorbance of BDPN NPs, BDPC NPs and BDPJ NPs was decreased by less than 20% after 16 min irradiation, while the absorbance of BDPI NPs was decreased as rapidly as that of ICG (Fig. 2a and Fig. S26,

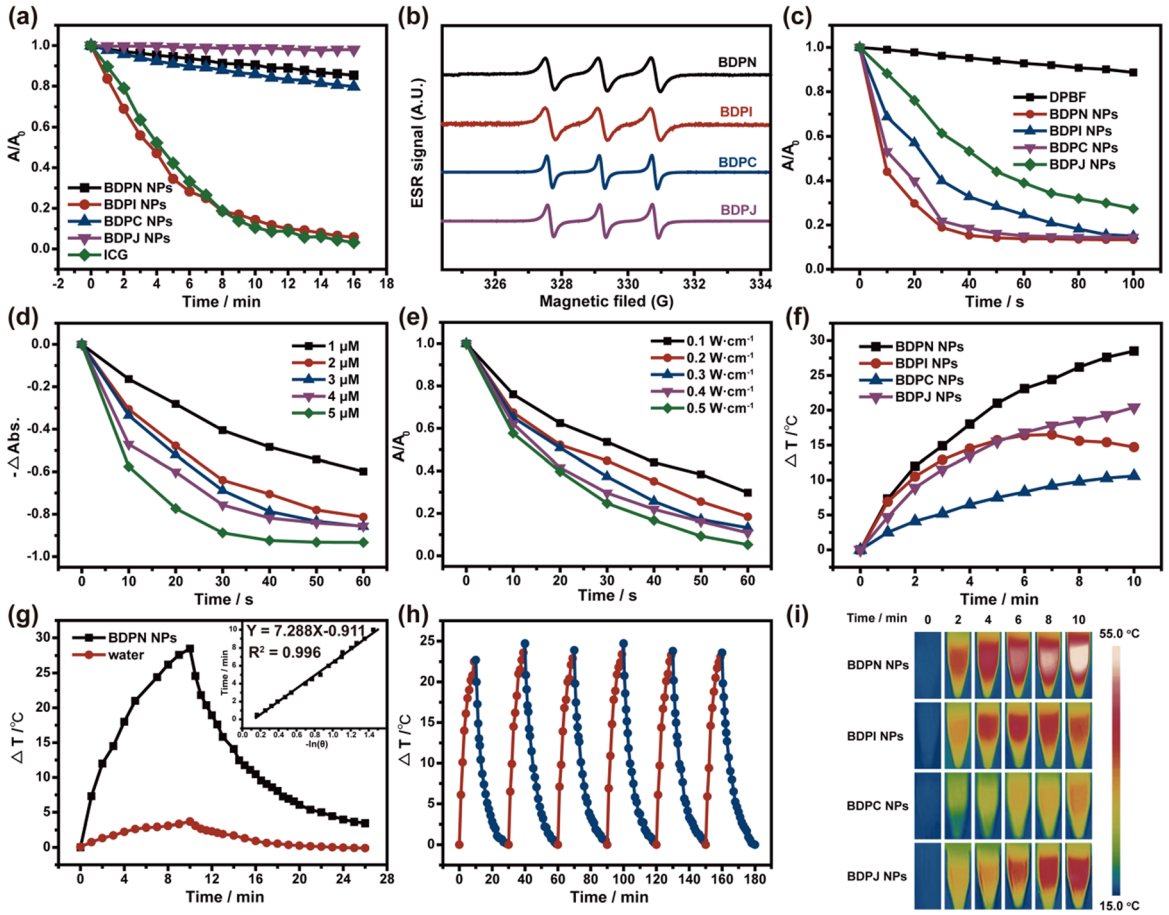

Fig. 2 (a) The absorbance changes of BDPN NPs, BDPI NPs, BDPC NPs, BDPJ NPs and ICG under 808 nm irradiation (0.5 W cm^{-2}, 16 min) at maximum absorption peak. (b) ESR spectra of $^1O_2$ generation captured by TEMPO under 808 nm irradiation. (c) The $^1O_2$ generation of BDPN NPs, BDPI NPs, BDPC NPs, BDPJ NPs (5 μM) using DPBF as a $^1O_2$ probe under 808 nm irradiation (0.1 W cm^{-2}). The $^1O_2$ generation of BDPN NPs at different concentrations (d) or laser powers (e). (f) The temperature changes and (i) thermal images of BDPN NPs, BDPI NPs, BDPC NPs and BDPJ NPs (30 μM) under 808 nm laser irradiation (0.5 W cm^{-2}) at different time intervals. (g) The temperature curves of BDPN NPs exposed to 808 nm laser (0.5 W cm^{-2}, 10 min) and subsequently natural cooling (Inset: Linear fitting of $-\ln\theta$ and time). (h) Photothermal stability study of BDPN NPs (30 μM) during six irradiation/cooling cycles under 808 nm laser irradiation (0.5 W cm^{-2}).

ESI†). Subsequently, electron spin resonance (ESR) spectroscopy was used to determine the type of ROS produced, using 5,5-dimethyl-1-pyrrolenoxide (DMPO) and 2,2,6,6-tetramethylpiperidine (TEMP) as the $O_2^{-\bullet}$/$^\bullet$OH probe and the $^1O_2$ probe, respectively.[48] After 808 nm laser irradiation, a typical triple peak of 2,2,6,6-tetramethylpiperidine-1-oxyl (TEMPO) appeared, but the characteristic peak of $O_2^{-\bullet}$/$^\bullet$OH captured by DMPO did not be observed, proving that $^1O_2$ was the only ROS species produced by the NPs upon light irradiation (Fig. 2b and Fig. S22, ESI†). The generation of $^1O_2$ by NPs is one of the principal parameter in PDT, and PDT efficacy is assessed by the rate of singlet oxygen production. The $^1O_2$ production rate of NPs under laser irradiation (808 nm, 0.1 W cm^{-2}) was investigated by observing the change in absorbance at 415 nm using 1,3-diphenylisobenzofuran (DPBF) as an indicator. As shown in Fig. 2c and Fig. S23 (ESI†), a significant decrease in DPBF absorption at 415 nm occurred, proving that they generated a large amount of $^1O_2$ under laser irradiation, and BDPN NPs and BDPC NPs exhibited better ROS generation abilities. Represented by BDPN NPs, the production rate of $^1O_2$ was found to be dependent on concentration and power (Fig. 1d, e and Fig. S24, 25, ESI†). The singlet oxygen quantum yield of these NPs was detected to quantitatively assess the efficiency of $^1O_2$ production and ICG was used as a standard (Φ_Δ = 0.14% in water). The singlet oxygen quantum yields of BDPN NPs, BDPI NPs, BDPC NPs and BDPJ NPs in water were calculated to be 40.76%, 46.88%, 88.23% and 9.33%, respectively (Fig. S27, ESI†). Although both BDPN NPs and BDPC NPs had similar rates of $^1O_2$ production, the value of BDPC NPs was much higher than that of BDPN NPs, resulting from the low absorbance of BDPC NPs at 808 nm. According to the ΔE_{ST} (Fig. 1a and Table S1, ESI†), BDPJ NPs should have better singlet oxygen productions, but BDPJ NPs turned out to have poor $^1O_2$ production capacities, which can also indirectly indicate that *J*-aggregation occurred. Additionally, all NPs retained different $^1O_2$ production capabilities, which could also indicate that there are still free molecules in the cavities of the formed NPs.

Radiation transition and ISC process were suppressed due to the occurrence of *J*-aggregation, so *J*-aggregates contributed to a non-radiative transition that generated a large amount of heat, promoting us to probe the phototransformation behaviour of NPs. The temperature elevation of four NPs (30 μM) under laser irradiation (808 nm, 0.5 W cm^{-2}) for 10 minutes were examined by thermal imaging technology. These results showed that the temperature rise (ΔT) of BDPN NPs was about 29 °C, which is 18 °C and 8 °C higher than that of BDPC NPs or BDPJ NPs at the same concentration (Fig. 2f and i). The PCE values of BDPN NPs, BDPC NPs and BDPJ NPs were calculated to be 54.9%, 21.45% and 30.07%, respectively (Fig. 2g and Fig. S29, ESI†). However, due to the poor photostability of BDPI NPs, the temperature started to drop after 6 minutes of laser irradiation, indicating that most of the BDPI NPs were destroyed and unsuitable for further tumor imaging and therapy. Above all, BDPN NPs had the ability to combine PDT and PTT. The therapeutic effect of BDPJ NPs was dominated by PTT, which had some photothermal conversion capability, but it still exhibited lower absorbance and photothermal conversion efficiency compared to BDPN NPs. BDPC NPs mainly reflected the PDT efficacy due to low temperature rise and low PCE. Taking BDPN NPs with the best photothermal performance as a representative, it was found that BDPN NPs were also concentration-dependent and power-dependent (Fig. S28, ESI†). Furthermore, we examined the photothermal stability of BDPN NPs, BDPC NPs and BDPJ NPs by means of five hot/cold cycles (Fig. 2h and Fig. S30, ESI†). The temperature elevation of BDPN NPs and BDPJ NPs remained almost constant over 5 cycles of 808 nm laser irradiation, indicating inappreciable damping of the photothermal conversion capacity. In contrast, BDPC NPs had poor photothermal stability because the temperature couldn't rise to a similar degree after laser irradiation. Based on the above experiments, it can be summarized that BDPN NPs are outstanding candidates for cancer diagnosis and treatment under synergistic phototherapy.

Antitumor therapy *in vitro*

Good internalisation is a prerequisite for achieving effective phototherapy and imaging. Thus, BDPN NPs, BDPC NPs and BDPJ NPs were further investigated biologically due to the poor photostability of BDPI NPs. First, they (1 μg mL^{-1}) were evaluated for internalisation by 4T1 tumor cells (Fig. 3a).

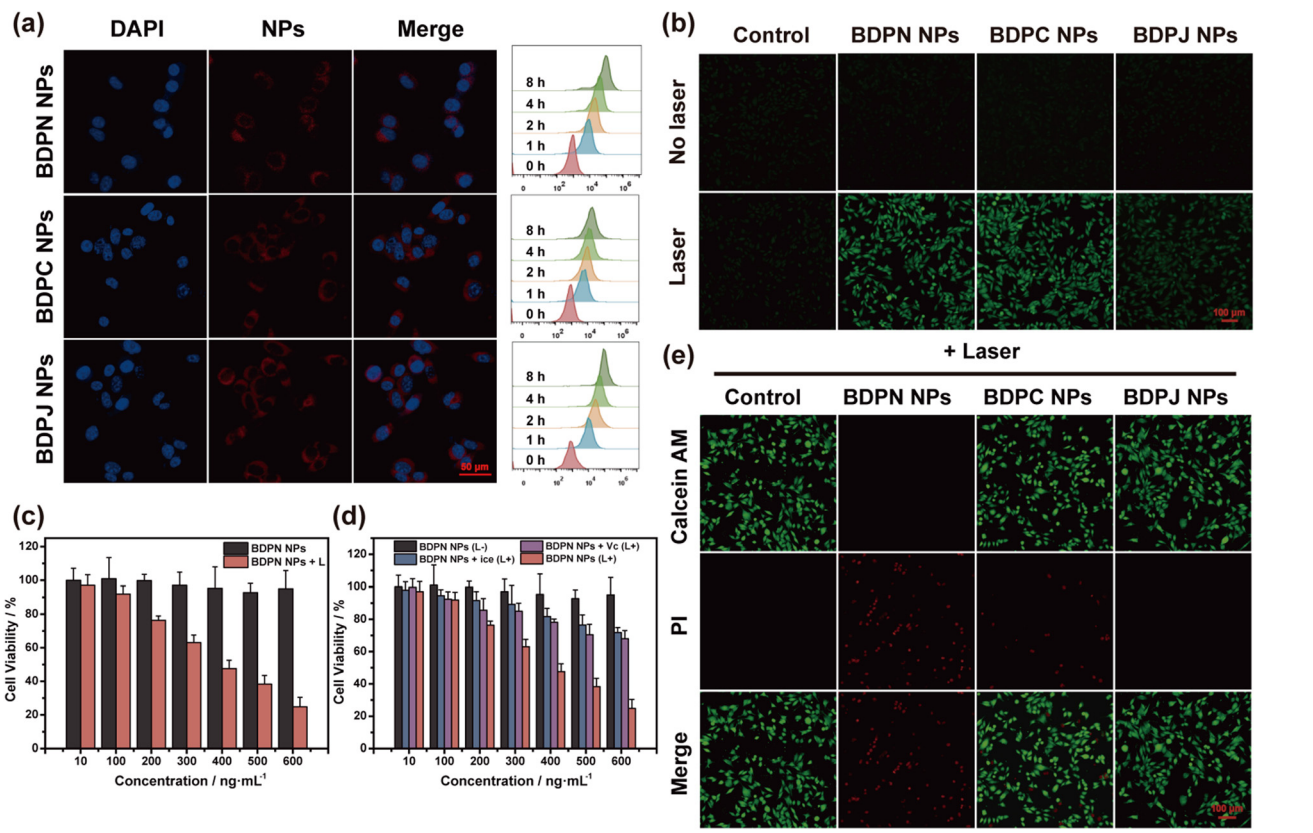

Fig. 3 (a) CLSM imagesof 4T1 tumor cells treated with BDPN NPs, BDPC NPs and BDPJ NPs for 4 h and processed fo rdifferent times for flow cytometry analysis (Scale bar: 50 μm). (b) ROS generation of BDPN NPs, BDPC NPs and BDPJ NPs using DCFH-DA as an indicator in 4T1 tumor cells under 808 nm laser irradiation (1.0 W cm^{-2}, 1 min) (Scale bar: 100 μm). (c) Cell viability of 4T1 tumor cells treated with BDPN NPs at different concentrations under laser irradiation (1.0 W cm^{-2}, 3 min) or darkness. (d) Cell viability of 4T1 tumor cells treated with BDPN NPs under laser irradiation or darkness, or laser irradiation together with VC (1.0×10^{-3} M) or ice bath. (e) Live/dead costaining images of 4T1 tumor cells treated with BDPN NPs, BDPC NPs and BDPJ NPs (0.6 μg mL^{-1}) under laser irradiation (1.0 W cm^{-2}, 3 min) (Scale bar: 100 μm).

Intracellular distribution in 4T1 tumor cells was observed by confocal laser scanning microscopy (CLSM). It could be observed that all three NPs (red fluorescence) were mainly internalised into the cytoplasm outside the nucleus (blue fluorescence, stined by Hoechst 33342). Then, the cell uptake of them in 4T1 tumor cells at different times was further explored by flow cytometry. With the increase of incubation times, the fluorescence values in the collected cells were increased, indicating that NPs were gradually being taken up by 4T1 tumor cells. Furthermore, most of the NPs were largely taken up by 4T1 tumor cells after two hours of incubation.

Excellent photosensitizers should have the characteristics of high level of phototoxicity and low level of dark toxicity. Thus, we determined the phototoxicity and dark toxicity of three NPs by MTT assays. Different concentrations of BDPN NPs, BDPC NPs and BDPJ NPs were incubated with 4T1 tumor cells for 24 h, followed by darkness/laser irradiation (808 nm, 1.0 W cm^{-2}) treatment, respectively. According to Fig. 3c and Fig. S31a, b (ESI†), both BDPN NPs and BDPJ NPs exhibited negligible cytotoxicity, whereas BDPC NPs showed significant concentration-dependent dark toxicity in the darkness. BDPN NPs demonstrated extremely strong photocytotoxicity at lower concentrations (0.6 μg mL^{-1}) under 3 min of laser irradiation. In contrast, the photocytotoxicity of BDPC NPs and BDPJ NPs increased with increasing concentrations, but remained weaker compared to BDPN NPs. The IC_{50} values for BDPN NPs, BDPC NPs and BDPJ NPs were calculated to be 0.40 μg mL^{-1}, 0.96 μg mL^{-1} and 2.23 μg mL^{-1}, respectively. Clearly, BDPN NPs exhibited better phototoxicity and dark toxicity compared to BDPC NPs and BDPJ NPs, and we speculated that BDPN NPs have a better synergistic phototherapeutic effect. To further distinguish the killing effects of single PDT or PTT on 4T1 tumor cell, we investigated the photocytotoxicity of NPs with ROS scavenger Vitamin C (VC) and ice bath, respectively (Fig. 3d and Fig. S31c, d, ESI†). The addition of VC effectively blocked the PDT effect, and increased the IC_{50} values of BDPN NPs, BDPC NPs and BDPJ NPs to 0.92 μg mL^{-1}, 1.29 μg mL^{-1} and 2.42 μg mL^{-1}. Similarly, temporary incubation of 4T1 tumor cells at 4 °C during laser irradiation effectively blocked the PTT effect, and the IC_{50} values of BDPN NPs, BDPC NPs and BDPJ NPs were increased to 1.11 μg mL^{-1}, 1.02 μg mL^{-1}, and 3.16 μg mL^{-1}, respectively. The presence of PDT/PTT synergistic effect on photocytotoxicity of NPs could be determined by calculating the association index (CI), and the calculated CI of BDPN NPs is 0.86 ($CI < 1.0$ is considered synergistic), while those of BDPC NPs and BDPJ NPs are 1.68 and 1.63, indicating the absence of synergy. To further corroborate the presence of synergistic phototherapy, we examined intracellular ROS production using 2,7-dichlorodihydrofluorescein diacetate (DCFH-DA) as an intracellular $^1O_2$ probe. Under the same laser irradiation time, bright green fluorescence could be observed in both BDPN NPs-treated and BDPC NPs-treated groups, while very weak green fluorescence was detected in the BDPJ NPs-treated group (Fig. 3b). This result was similar to the production of $^1O_2$ by nanoparticles in aqueous solution. Although both BDPN NPs and BDPC NPs showed better $^1O_2$ production, the cell survival rate of BDPN NPs in the MTT assays was lower than that of BDPC NPs, which indirectly suggested that BDPN NPs have better PTT ability. Thus, the high phototoxicity and no dark cytotoxicity demonstrated that BDPN NPs can be used as an effective PS for the synergistic phototherapy.

Furthermore, in order to visually observe the phototherapeutic effect of BDPN NPs, BDPC NPs and BDPJ NPs, the combined live/dead cell staining assay was performed on 4T1 tumor cells using calcein AM (green, live cells) and PI (red, dead cells), thus achieving the visualisation of cell viability. Firstly, the photocytotoxicity and dark cytotoxicity of these NPs (0.6 μg mL^{-1}) were investigated by fluorescent microscope. According to Fig. 3e and Fig. S32 (ESI†), the 4T1 tumor cells treated with BDPN NPs and BDPJ NPs in the darkness exhibited the same green fluorescence as the control group with almost no death, which also visually demonstrated the good dark toxicity of BDPN NPs and BDPJ NPs. However, sporadic red fluorescence in the BDPC NPs-treated group indicated that BDPC NPs remained toxic at this concentration, resulting in a small amount of cell deaths. In contrast, under 808 nm laser irradiation (1.0 W cm^{-2}), the BDPN NPs-treated group exhibited significant red fluorescence, indicating that the intense phototoxicity of BDPN NPs killed almost all the cells, and the increased red fluorescence in the BDPC NPs-treated group indicated the presence of a slight phototherapeutic effect. However, the BDPJ NPs-treated group still exhibited strong green fluorescence, remaining no significant apoptosis. Subsequently, the photocytotoxicity and dark cytotoxicity of BDPC NPs (1.0 μg mL^{-1}) and BDPJ NPs (2.0 μg mL^{-1}) at IC_{50} were assayed (Fig. S33, ESI†). Under 808 nm laser irradiation (1.0 W cm^{-2}), both BDPC NPs-treated and BDPJ NPs-treated groups showed nearly half of the cells death. The results of live/dead cell staining assay were in good agreement with the results of the MTT assay and provided further evidence that BDPN NPs had a good phototherapeutic effect at lower concentrations.

Multimodal imaging *in vivo*

To verify the efficacy of BDPN NPs, BDPC NPs and BDPJ NPs *in vivo*, a well-established 4T1 xenograft mouse model was employed. The imaging and treatment effects were investigated by *in situ* injection of the three NPs (0.15 mg kg^{-1}) into 4T1 tumor-bearing mice under 808 nm (1.0 W cm^{-2}) laser irradiation. Firstly, *in vivo* NIR fluorescence imaging was explored by cutting off the wavelengths below 900 nm through an optical low-pass filter (OLPF) to acquire the tumor fluorescence emission signal at different time points (Fig. 4b and d). The fluorescence at the tumor site was gradually enhanced and reached a maximum at 24 h after injection, indicating that the nanoparticles were gradually taken up by the 4T1 tumor cells. BDPN NPs and BDPC NPs showed a slightly stronger NIR fluorescence imaging capability, which is more consistent with the fluorescence quantum yields of them in water. Then, the fluorescence was gradually diminished, but still showed after 48 hours, suggesting that these NPs have strong tumor retention and stable bioimaging capabilities, allowing real-time monitoring of the drugs and timely feedback on treatment.

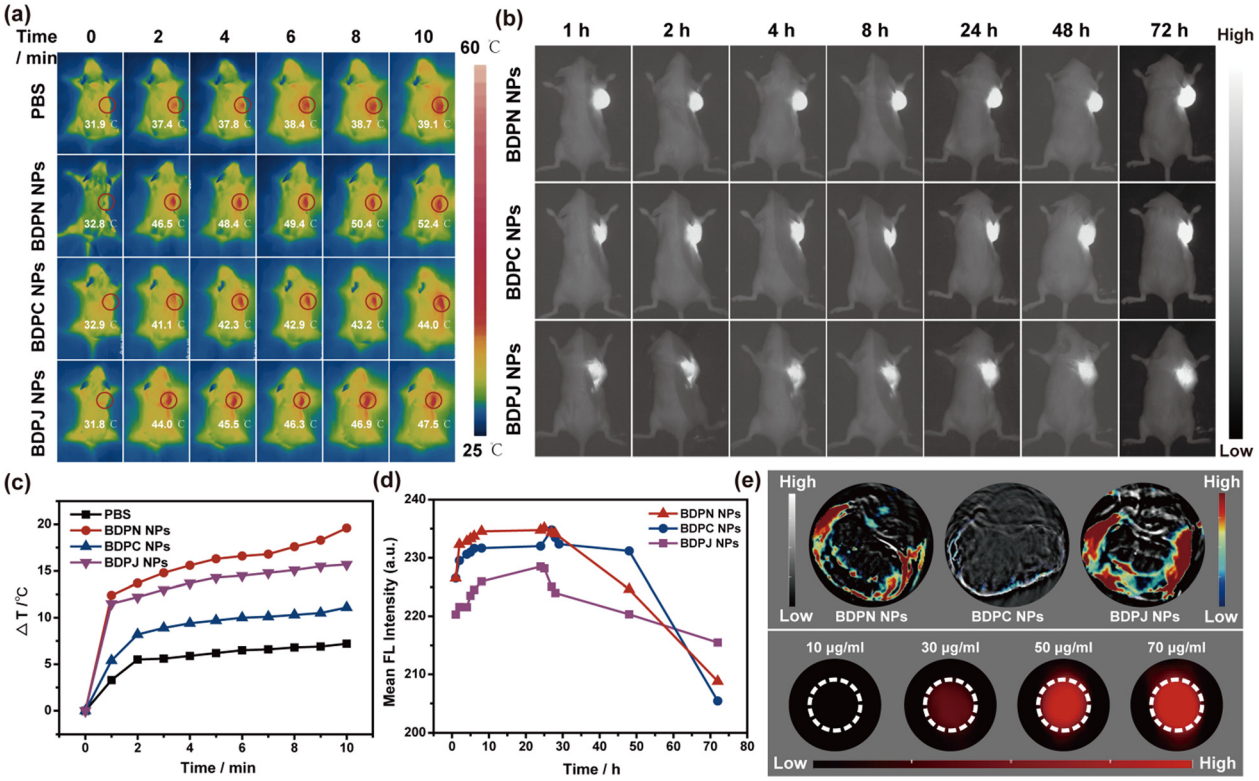

Fig. 4 (a) Infrared thermal images and (c) temperature elevation at the tumor sites recorded for 4T1 tumor-bearing mice injected with PBS, BDPN NPs, BDPC NPs and BDPJ NPs under 808 nm laser irradiation (1.0 W cm^{-2}), respectively. (b) Fluorescence images and (d) mean fluorescence intensity at the tumor sites recorded for 4T1 tumor-bearing mice injected with BDPN NPs, BDPC NPs and BDPJ NPs under an 808 nm excitation filter (1.0 W cm^{-2}) and 900 nm emission filter, respectively. (e) PA images at the tumor of the mice treated with BDPN NPs, BDPC NPs and BDPJ NPs, and PA images of BDPN NPs at different concentrations.

To explore PTT effect *in vivo*, we monitored the temperature changes at tumor site in mice under 808 nm laser irradiation (1.0 W cm^{-2}, 10 min) with a thermography. Notably, temperature of the tumor site in the PBS-treated group was only increased by approximately 7 °C after 10 min laser irradiation, while that in the BDPN NPs-treated, BDPC NPs-treated and BDPJ NPs-treated groups was increased by approximately 20 °C, 11 °C and 17 °C, respectively (Fig. 4a and c). Because of their high photothermal conversion efficiency, BDPN NPs and BDPJ NPs have shown excellent photothermal therapeutic capabilities and photothermal imaging capabilities *in vivo*. In addition, the PA signal is a pressure wave generated by thermal expansion, which is caused by the release of heat from the PS at the tumor by laser irradiation. Therefore, PA signals usually accompany the PTT process. Subsequently, we examined the PAI capability of the NPs *in vivo*. BDPN NPs and BDPJ NPs had better PAI capabilities with a better signal-to-back ratio, while BDPC NPs had weaker signals due to lower PCE, and the results were consistent with PTT effect (Fig. 4e). Furthermore, we have also observed that the PA signal generated by NPs displayed the concentration dependent in the tissue simulation experiment (Fig. 4e and Fig. S35, ESI†). All the above results showed that NPs with multimodal imaging, including NIR FLI/PTI/PAI, had great promise in accurately guiding phototherapy *in vivo*.

Antitumor therapy *in vivo*

Encouraged by the astonishing phototherapy effect *in vitro*, the anticancer capability of BDPN NPs, BDPC NPs and BDPJ NPs was inspected in the 4T1 tumor-bearing mice. The mice bearing 4T1 tumors were randomly split into 8 groups (n = 6 per group) for different treatments, and the efficacy and drug safety of the combination therapy were also assessed by measuring the tumor size and mice weight at different times (Fig. 5a and b). Tumor volumes were increased about 11-fold in all non-laser groups, indicating no effect on tumor growth in the absence of laser-activated drugs. In the 808 nm laser irradiation group, tumor volumes were increased approximately 9-fold in the PBS-treated group, demonstrating that laser irradiation alone without drugs was unable to inhibit the tumor growth. In contrast, in the laser-irradiated BDPC NPs-treated group, the tumor growth was slowed and began to ablate on the 10th day of treatment, eventually increasing by about 3 times due to the limited absorption of NPs at 808 nm and only PDT effect. However, tumors in the BDPN NPs-treated group and BDPJ NPs-treated group began to ablate on day 6 and 8 of treatment under laser irradiation, respectively. Moreover, the laser-irradiated BDPN NPs-treated group demonstrated fastest tumor treatment efficiency, which proved the effectiveness of the combined PDT/PTT treatment.

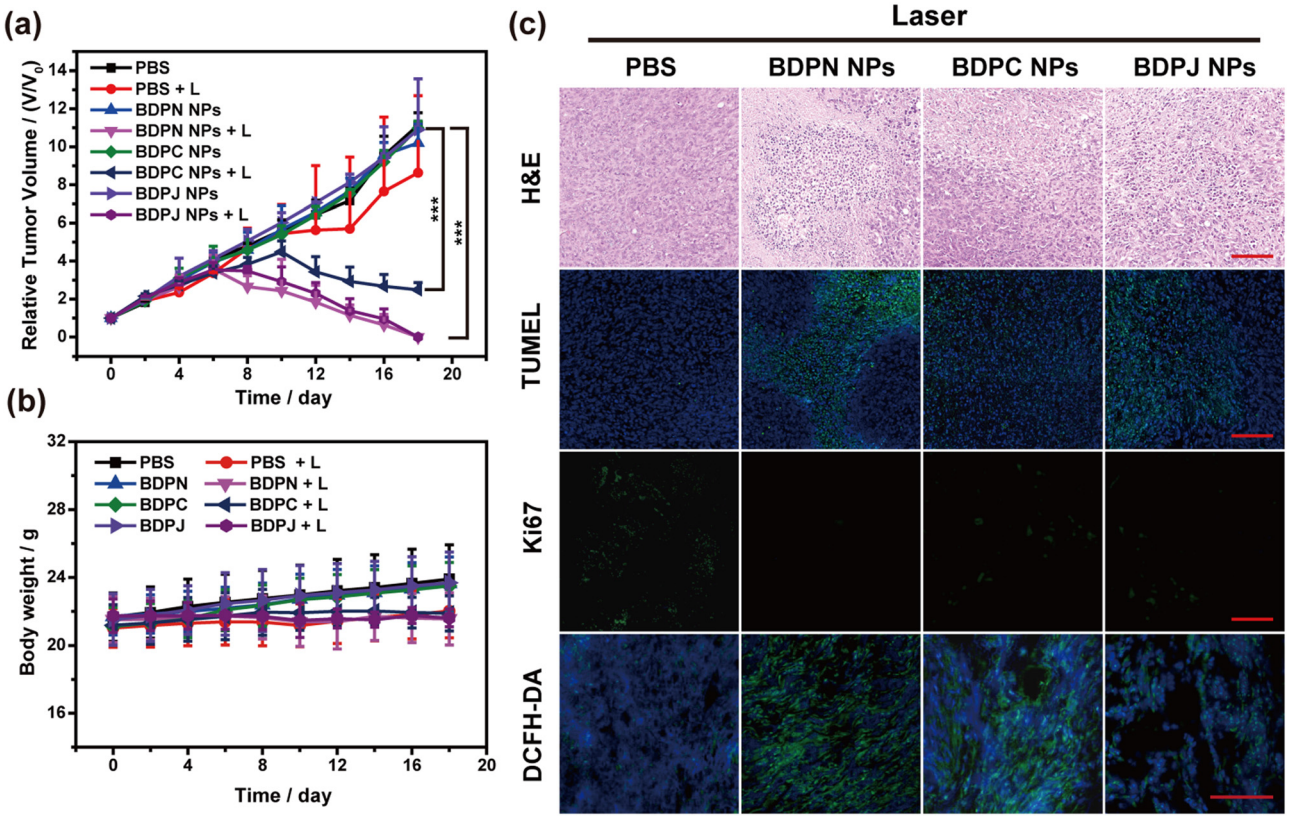

Fig. 5 (a) Tumor growth profile of the mice in different treatment groups. Significance (*$p < 0.05$, **$p < 0.01$, ***$p < 0.001$) was verified by one-way ANOVA. (b) Body weight of the mice in different treatment groups. (c) H&E, TUNEL, Ki67 staining and DCFH-DA analysis of tumor sections from 4T1 tumor-bearing mice treated with PBS, BDPN NPs, BDPC NPs and BDPJ NPs under 808 nm laser irradiation (1.0 W cm^{-2}, 5 min), respectively. All the scale bars are 100 μm.

To further validate the efficacy of PDT *in vivo*, the production of $^1O_2$ was examined in excised tumors tissue using DCFH-DA as a ROS indicator. As shown in Fig. 5c and Fig. S36 (ESI†), the laser-irradiated BDPN NPs-treated group showed brighter green fluorescence, demonstrating that more $^1O_2$ in the tumor tissue and better PDT effect. Additionally, BDPC NPs also had good PDT effect, which were consistent with the results of *in vitro* experiments. Subsequently, the antitumor efficacy of BDPN NPs, BDPC NPs and BDPJ NPs was analyzed. Hematoxylin-eosin (H&E) staining was performed on the excised tumors for histopathological analysis (Fig. 5c and Fig. S36, ESI†). There were more tumor necrotic areas in the laser-irradiated BDPN NPs-treated and laser-irradiated BDPJ NPs-treated groups than the laser-irradiated BDPC NPs-treated group which were represented by cell volume reduction, nucleoplasmic condensation and nucleolus fragmentation of the nuclear membrane. The results were further confirmed by the TUNEL staining experiment (Fig. 5c and Fig. S36, ESI†). The tumor tissues in the laser-irradiated BDPN/BDPJ NPs-treated groups exhibited more apoptotic signals. Subsequently, Ki67 staining, a marker of cell proliferation, showed more cell proliferation in the groups without laser irradiation, while the tumor groups with both BDPN NPs and laser showed almost no proliferation and highest levels of apoptotic (Fig. 5c and Fig. S36, ESI†). Based on the above series of *in vivo* tests, it demonstrated that BDPN NPs had the best synergistic effect of PDT and PTT, leading to rapid tumor ablation.

Biosafety analysis

During the 18-day observation, the mice in the no-laser groups all showed a slight increase in body weight due to tumor growth, while the laser-irradiated mice showed no significant change in body weight (Fig. 5b), indicating that BDPN NPs, BDPC NPs and BDPJ NPs all have good biosafety *in vivo*. In addition, to assess the biocompatibility of the NPs, major organs (heart, liver, spleen, lungs and kidneys) of the executed mice were taken for H&E staining. As shown in Fig. 6 and Fig. S37 (ESI†), there was no significant difference in the morphology of the major organs among the 8 groups, suggesting negligible cell and tissue damages. Furthermore, the blood of the mice was used for blood routine analysis and blood biochemistry. No obvious changes were observed in the blood hematology (Fig. S39, ESI†) and blood biochemistry (Fig. S38, ESI†) of all groups of the mice, suggesting the excellent biocompatibility of the as-prepared NPs. The above results collectively verified that the as-prepared BDPN NPs were a class of preeminent PSs with favorable biosafety and therapeutic

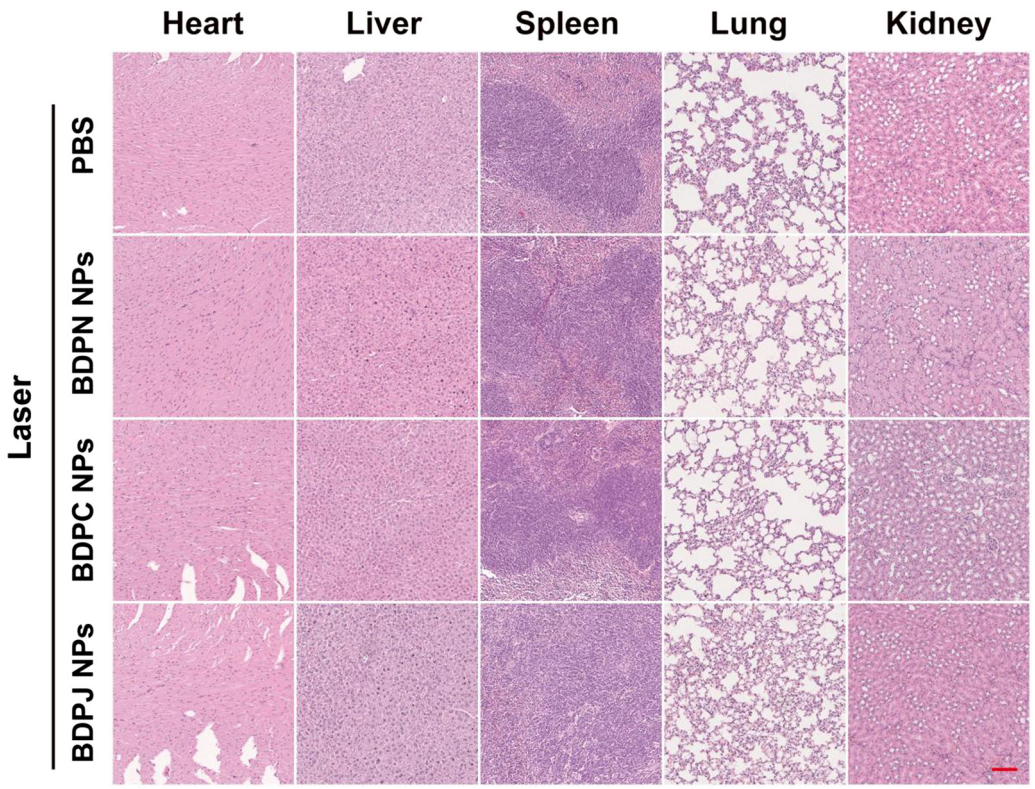

Fig. 6 H&E staining of major organs (including heart, liver, spleen, lung and kidney) from the mice treated with PBS, BDPN NPs, BDPC NPs and BDPJ NPs under 808 nm laser irradiation (1.0 W cm^{-2}, 5 min) after 18 days, respectively. All the scale bars are 100 μm.

efficacy, which had potential to multiple imaging-guided synergistic PDT/PTT.

Conclusions

In summary, we had successfully introduced different electronic structures at the 3,5-positions of BODIPY to form four amphiphilic iodine-containing BODIPYs with D–A–D structure. Stable nanoparticles (BDPN NPs, BDPI NPs, BDPC NPs and BDPJ NPs) were informed in water by self-assembly, and *J*-aggregation existed in different degrees due to the introduction of hydrophilic chains and iodine atoms. Satisfyingly, the formed NPs did not aggregate completely, and there were still free molecules in the nano-cavities, making it possible to combine FLI/PTI/PAI/PDT/PTT. As expected, the self-assembled BDPN NPs were able to promote an optimum balance between fluorescence, photothermal and photodynamic properties, and exhibited high fluorescence quantum yields (3.0%), PCE (54.9%) and $^1O_2$ production (40.76%). More importantly, BDPN NPs exhibited excellent FLI/PTI/PAI-guided PTT/PDT synergistic therapeutic capabilities both *in vitro* and *in vivo*, whereas BDPC NPs and BDPJ NPs could not possess all the capabilities synchronously. In addition, BDPN NPs also displayed good biocompatibility. This work had exploited a prospective BODIPY nanoparticles through hydrophilic and halogen bonding interactions that contribute to effective, safe and versatile cancer theranostics. Further, more precise therapeutically integrated nanomedicines can be developed by improving the targeting and optical penetration depth of multifunctional nanoparticles.

Author contributions

The manuscript was written through contributions of all authors. All authors have given approval to the final version of the manuscript.

Conflicts of interest

There are no conflicts to declare.

Acknowledgements

This study was supported by the National Natural Science Foundation of China (grant numbers 21971049 and 51903070), the Zhejiang Provincial Natural Science Foundation of China (grant numbers LZ23B040001 and LY23E030003), and ''Ten-thousand Talents Plan'' of Zhejiang Province (grant number 2019R52040).

Notes and references

1 J. A. Krall, F. Reinhardt, O. A. Mercury, D. R. Pattabiraman, M. W. Brooks, M. Dougan, A. W. Lambert, B. Bierie,

H. L. Ploegh, S. K. Dougan and R. A. Weinberg, The systemic response to surgery triggers the outgrowth of distant immune-controlled tumors in mouse models of dormancy, *Sci. Transl. Med.*, 2018, **10**, eaan3464.
2 B. Stea and R. S. Witte, Introduction to novel developments in radio-imaging and radiotherapy, *Clin. Exp. Metastasis*, 2022, **39**, 219–224.
3 N. Behranvand, F. Nasri, R. Zolfaghari Emameh, P. Khani, A. Hosseini, J. Garssen and R. Falak, Chemotherapy: a double-edged sword in cancer treatment, *Cancer Immunol. Immunother.*, 2022, **71**, 507–526.
4 H. Y. Min and H. Y. Lee, Molecular targeted therapy for anticancer treatment, *Exp. Mol. Med.*, 2022, **54**, 1670–1694.
5 J. Funkhouser, Reinventing pharma: The theranostic revolution, *Current Drugs Discovery*, 2002, **2**, 17–19.
6 A. Borchers and T. Pieler, Programming pluripotent precursor cells derived from Xenopus embryos to generate specific tissues and organs, *Genes*, 2010, **1**, 413–426.
7 Y. Shetty, P. Prabhu and B. Prabhakar, Emerging vistas in theranostic medicine, *Int. J. Pharm.*, 2019, **558**, 29–42.
8 D. Wang, M. M. S. Lee, W. Xu, R. T. K. Kwok, J. W. Y. Lam and B. Z. Tang, Theranostics based on AIEgens, *Theranostics*, 2018, **8**, 4925–4956.
9 S. Alshehri, S. S. Imam, M. Rizwanullah, S. Akhter, W. Mahdi, M. Kazi and J. Ahmad, Progress of Cancer Nanotechnology as Diagnostics, Therapeutics, and Theranostics Nanomedicine: Preclinical Promise and Translational Challenges, *Pharmaceutics*, 2020, **13**, 24–58.
10 L. Zhang, H.-M. Li, Y. Zhao, L.-J. Zhou, Y. Liu, F.-L. Jiang, Y. Liu and P. Jiang, Tuning long-term mitochondrial imaging and photodynamic therapy capabilities through rational design of aggregation-induced emission luminogens, *Sens. Actuators, B*, 2022, **368**, 132213.
11 T. Zhao, X. Hu, R. Ma, F. Dong, T. Liu, L. Li, H. Yan, Y. Xu, W. Liu, B. Zou and B. Tang, Photovoltaic polymer Photosensitizer-Doped Nano-Therapeutic reagent for in vivo enhanced bioimaging guided photodynamic therapy, *Chem. Eng. J.*, 2022, **441**, 135983.
12 Y. Chen, S. Zhang, T. Cheng, W. Lin, L. Mao, Z. Chen, Y. Yang, H. Huang, J. Li, Z. Ke and Z.-K. Cui, Design and development of a mitochondrial-targeted photosensitizer for two-photon fluorescence imaging and photodynamic therapy, *J. Mater. Sci. Technol.*, 2023, **141**, 135–148.
13 S. Qi, N. Kwon, Y. Yim, V. N. Nguyen and J. Yoon, Fine-tuning the electronic structure of heavy-atom-free BODIPY photosensitizers for fluorescence imaging and mitochondria-targeted photodynamic therapy, *Chem. Sci.*, 2020, **11**, 6479–6484.
14 Y. Yang, Z. Zeng, E. Almatrafi, D. Huang, C. Zhang, W. Xiong, M. Cheng, C. Zhou, W. Wang, B. Song, X. Tang, G. Zeng, R. Xiao and Z. Li, Core-shell structured nanoparticles for photodynamic therapy-based cancer treatment and related imaging, *Coord. Chem. Rev.*, 2022, **458**, 214427.
15 V. N. Nguyen, Y. Yan, J. Zhao and J. Yoon, Heavy-Atom-Free Photosensitizers: From Molecular Design to Applications in the Photodynamic Therapy of Cancer, *Acc. Chem. Res.*, 2021, **54**, 207–220.
16 G. Li, Q. Wang, J. Liu, M. Wu, H. Ji, Y. Qin, X. Zhou and L. Wu, Innovative strategies for enhanced tumor photodynamic therapy, *J. Mater. Chem. B*, 2021, **9**, 7347–7370.
17 L. Gao, R. Liu, F. Gao, Y. Wang, X. Jiang and X. Gao, Plasmon-Mediated Generation of Reactive Oxygen Species from Near-Infrared Light Excited Gold Nanocages for Photodynamic Therapy in Vitro, *ACS Nano*, 2014, **8**, 7260–7271.
18 J. Du, T. Shi, S. Long, P. Chen, W. Sun, J. Fan and X. Peng, Enhanced photodynamic therapy for overcoming tumor hypoxia: From microenvironment regulation to photosensitizer innovation, *Coord. Chem. Rev.*, 2021, **427**, 213604.
19 L. Huang, S. Zhao, J. Wu, L. Yu, N. Singh, K. Yang, M. Lan, P. Wang and J. S. Kim, Photodynamic therapy for hypoxic tumors: Advances and perspectives, *Coord. Chem. Rev.*, 2021, **438**, 213888.
20 F. Wei, T. W. Rees, X. Liao, L. Ji and H. Chao, Oxygen self-sufficient photodynamic therapy, *Coord. Chem. Rev.*, 2021, **432**, 213714.
21 J. Chen, C. Ning, Z. Zhou, P. Yu, Y. Zhu, G. Tan and C. Mao, Nanomaterials as photothermal therapeutic agents, *Prog. Mater. Sci.*, 2019, **99**, 1–26.
22 B. Li, H. Shao, L. Gao, H. Li, H. Sheng and L. Zhu, Nanodrug co-delivery system of natural active ingredients and chemotherapy drugs for cancer treatment: a review, *Drug Delivery*, 2022, **29**, 2130–2161.
23 X. Lin, F. Chen, X. Yu, H. Wang, H. Qiu, Y. Li, S. Yin and P. J. Stang, Phenylthiol-BODIPY-based supramolecular metallacycles for synergistic tumor chemo-photodynamic therapy, *Proc. Natl. Acad. Sci. U. S. A.*, 2022, **119**, e2203994119.
24 J. Zhang, Y. Li, M. Jiang, H. Qiu, Y. Li, M. Gu and S. Yin, Self-Assembled Aza-BODIPY and Iron(III) Nanoparticles for Photothermal-Enhanced Chemodynamic Therapy in the NIR-II Window, *ACS Biomater. Sci. Eng.*, 2023, **9**, 821–830.
25 Y. Li, X. Liu, X. Zhang, W. Pan, N. Li and B. Tang, Immune Cycle-Based Strategies for Cancer Immunotherapy, *Adv. Funct. Mater.*, 2021, **31**, 2107540.
26 L. Liu, X. Wang, L. J. Wang, L. Guo, Y. Li, B. Bai, F. Fu, H. Lu and X. Zhao, One-for-All Phototheranostic Agent Based on Aggregation-Induced Emission Characteristics for Multimodal Imaging-Guided Synergistic Photodynamic/Photothermal Cancer Therapy, *ACS Appl. Mater. Interfaces*, 2021, **13**, 19668–19678.
27 B. Park, S. Park, J. Kim and C. Kim, Listening to drug delivery and responses via photoacoustic imaging, *Adv. Drug Delivery Rev.*, 2022, **184**, 114235.
28 Q. Tang, W. Xiao, C. Huang, W. Si, J. Shao, W. Huang, P. Chen, Q. Zhang and X. Dong, pH-Triggered and Enhanced Simultaneous Photodynamic and Photothermal Therapy Guided by Photoacoustic and Photothermal Imaging, *Chem. Mater.*, 2017, **29**, 5216–5224.
29 J. L. Wang, L. Zhang, M. J. Zhao, T. Zhang, Y. Liu and F. L. Jiang, Mitochondria-Targeted BODIPY Nanoparticles for Enhanced Photothermal and Photoacoustic Imaging In Vivo, *ACS Appl. Bio. Mater.*, 2021, **4**, 1760–1770.
30 T. Zhang, C. Ma, T. Sun and Z. Xie, Unadulterated BODIPY nanoparticles for biomedical applications, *Coord. Chem. Rev.*, 2019, **390**, 76–85.

31 A. N. Bismillah and I. Aprahamian, Fundamental studies to emerging applications of pyrrole-BF(2) (BOPHY) fluorophores, *Chem. Soc. Rev.*, 2021, **50**, 5631–5649.
32 A. Turksoy, D. Yildiz and E. U. Akkaya, Photosensitization and controlled photosensitization with BODIPY dyes, *Coord. Chem. Rev.*, 2019, **379**, 47–64.
33 W. Sun, X. Zhao, J. Fan, J. Du and X. Peng, Boron Dipyrromethene Nano-Photosensitizers for Anticancer Phototherapies, *Small*, 2019, **15**, e1804927.
34 V.-N. Nguyen, J. Ha, M. Cho, H. Li, K. M. K. Swamy and J. Yoon, Recent developments of BODIPY-based colorimetric and fluorescent probes for the detection of reactive oxygen/nitrogen species and cancer diagnosis, *Coord. Chem. Rev.*, 2021, **439**, 213936.
35 P. Kaur and K. Singh, Recent advances in the application of BODIPY in bioimaging and chemosensing, *J. Mater. Chem. B*, 2019, **7**, 11361–11405.
36 J. L. Donnelly, D. Offenbartl-Stiegert, J. M. Marin-Beloqui, L. Rizzello, G. Battaglia, T. M. Clarke, S. Howorka and J. D. Wilden, Exploring the Relationship between BODIPY Structure and Spectroscopic Properties to Design Fluorophores for Bioimaging, *Chemistry*, 2020, **26**, 863–872.
37 J. Zou, Z. Yin, P. Wang, D. Chen, J. Shao, Q. Zhang, L. Sun, W. Huang and X. Dong, Photosensitizer synergistic effects: D-A-D structured organic molecule with enhanced fluorescence and singlet oxygen quantum yield for photodynamic therapy, *Chem. Sci.*, 2018, **9**, 2188–2194.
38 Q. Wu, Y. Zhu, X. Fang, X. Hao, L. Jiao, E. Hao and W. Zhang, Conjugated BODIPY Oligomers with Controllable Near-Infrared Absorptions as Promising Phototheranostic Agents through Excited-State Intramolecular Rotations, *ACS Appl. Mater. Interfaces*, 2020, **12**, 47208–47219.
39 E. Y. Zhou, H. J. Knox, C. Liu, W. Zhao and J. Chan, A Conformationally Restricted Aza-BODIPY Platform for Stimulus-Responsive Probes with Enhanced Photoacoustic Properties, *J. Am. Chem. Soc.*, 2019, **141**, 17601–17609.
40 M. Su, S. Li, H. Zhang, J. Zhang, H. Chen and C. Li, Nano-Assemblies from J-Aggregated Dyes: A Stimuli-Responsive Tool Applicable To Living Systems, *J. Am. Chem. Soc.*, 2019, **141**, 402–413.
41 Z. Han, G. Czap, C.-L. Chiang, C. Xu, P. J. Wagner, X. Wei, Y. Zhang, R. Wu and W. Ho, Imaging the halogen bond in self-assembled halogenbenzenes on silver, *Science*, 2017, **358**, 206–210.
42 X. Yan, M. Su, Y. Liu, Y. Zhang, H. Zhang and C. Li, Molecularly Engineered Hierarchical Nanodisc from Antiparallel J-stacked BODIPY Conjugates: Application to Theranostics with Mutually Beneficial Properties, *Adv. Funct. Mater.*, 2020, **31**, 2008406.
43 X. Hu, H. Chen, L. Zhao, M. Miao and Y. Zheng, Observation of a Solid-State-Induced Thermally Populated Spin-Triplet State in Radical Regioisomers, *Chem. Mater.*, 2019, **31**, 10256–10262.
44 M. Su, Q. Han, X. Yan, Y. Liu, P. Luo, W. Zhai, Q. Zhang, L. Li and C. Li, A Supramolecular Strategy to Engineering a Non-photobleaching and Near-Infrared Absorbing Nano-J-Aggregate for Efficient Photothermal Therapy, *ACS Nano*, 2021, **15**, 5032–5042.
45 J. Zhang, M. Jiang, Y. Li, J. Yu, H. Qiu, M. Gu, Y. Li and S. Yin, Self-assembled boron dipyrromethene-based nanocarriers with encapsulated doxorubicin for chemo-photodynamic therapy, *Dyes Pigm.*, 2022, **206**, 110679.
46 D. Xi, N. Xu, X. Xia, C. Shi, X. Li, D. Wang, S. Long, J. Fan, W. Sun and X. Peng, Strong pi-pi Stacking Stabilized Nanophotosensitizers: Improving Tumor Retention for Enhanced Therapy for Large Tumors in Mice, *Adv. Mater.*, 2022, **34**, e2106797.
47 C. Yin, S. Wang, Q. Ren, X. Shen, X. Chen, Y. Liu and S. Liu, Radial extracorporeal shock wave promotes the enhanced permeability and retention effect to reinforce cancer nanothermotherapeutics, *Sci. Bull.*, 2019, **64**, 679–689.
48 L. Li, C. Shao, T. Liu, Z. Chao, H. Chen, F. Xiao, H. He, Z. Wei, Y. Zhu, H. Wang, X. Zhang, Y. Wen, B. Yang, F. He and L. Tian, An NIR-II-Emissive Photosensitizer for Hypoxia-Tolerant Photodynamic Theranostics, *Adv. Mater.*, 2020, **32**, e2003471.